COMMUNICATIONS PHYSICS

ARTICLE

DOI: 10.1038/s42005-018-0047-y OPEN

High-field nonlinear optical response and phase control in a dielectric laser accelerator

D. Cesar[1], S. Custodio[1], J. Maxson[1,3], P. Musumeci[1], X. Shen[1], E. Threlkeld[1], R.J. England[2], A. Hanuka[2], I.V. Makasyuk[2], E.A. Peralta[2], K.P. Wootton[2] & Z. Wu[2]

Advances in ultrafast laser technology and nanofabrication have enabled a new class of particle accelerator based upon miniaturized laser-driven photonic structures. However, developing a useful accelerator based on this approach requires control of the particle dynamics at field intensities approaching the damage limit. We measure acceleration in a fused silica dielectric laser accelerator driven by fields of up to 9 GV m^{-1} and observe a record 1.8 GV m^{-1} in the accelerating mode. At these intensities the dielectric is driven beyond its linear response and self-phase modulation changes the phase velocity of the accelerating mode, reducing the average gradient to 850 MeV m^{-1}. We show that free-space optics can be used to compensate this dephasing and demonstrate that tailoring the laser phase and amplitude can facilitate optimization of the beam dynamics. This could enable MeV scale energy gain in a single stage and pave the way towards applications in scientific, industrial, and medical fields.

[1] Department of Physics and Astronomy, UCLA, Los Angeles, CA 90095, USA. [2] SLAC National Accelerator Laboratory, Menlo Park, CA 94025, USA. [3] Present address: Department of Physics, Cornell University, Ithaca, NY 14850, USA. Correspondence and requests for materials should be addressed to D.C. (email: dcesar@ucla.edu)

Realizing future university-scale light sources, affordable next-generation high energy colliders, and ultra-compact medical and industrial linacs requires the development of new particle acceleration techniques that are more compact, energy efficient, and lower cost than current technology based on microwave cavities and high-power klystrons. A promising approach that has gained interest in recent years is the use of photonic structures, referred to as dielectric laser accelerators (DLA), fabricated from optically transparent materials and powered by ultrafast lasers[1]. In this scheme, the photonic structure mediates the transfer of energy from a laser to a particle beam. The shorter wavelength coupled with the ability of compact solid state lasers to generate peak fields in excess of 10 GV m^{-1}, leads to a large reduction in the size of the accelerator device. In addition, the processes used to fabricate these structures are amenable to inexpensive mass production. These features make DLA an attractive option, offering the potential for widely available compact high energy accelerators for a variety of applications in science and industry[2].

To this end, researchers have studied a variety of novel accelerating, focusing, and diagnostic structures[3–8], and have conducted experimental demonstrations with various injected particle energies[9–14]. The primary goal of these initial efforts has been to optimize the structure designs to maximize the conversion of the incident laser field into accelerating gradient.

To achieve accelerating fields >1 GV m^{-1}, the structure must be driven at laser intensities approaching the damage limits of the material, where nonlinear optical effects can begin to perturb the spatial and temporal profile of the laser field. At the same time, designing a compact all-optical accelerator requires precise understanding and control of both amplitude and phase of the driving electromagnetic field along the interaction. In the experiment described here, we test the high field response and determine the dominant physical limitations on the achievable energy gain of the particles in a DLA prior to the onset of irreversible optical damage. The experiment uses an externally injected high brightness 8 MeV electron beam from the UCLA Pegasus photoinjector[15] to probe the accelerating fields in an enclosed vacuum channel within a double-grating fused silica structure. As the drive laser intensity is increased to >7 TW cm^{-2}, we observe the transition to a non-linear regime where electron energy gain and loss no longer scale linearly with the incident field amplitude. In a second set of measurements we demonstrate a pre-compensation scheme based on adding negative dispersion to shape the phase of the laser pulse to counteract the optical Kerr effect[16]. These observations, which are shown to be in excellent agreement with time and frequency-domain calculations, provide a fundamental step forward in the development of high gradient DLA accelerators.

Results

Measurement of electron energy spectrum. The electron based measurement of the accelerating fields in the DLA is illustrated in Fig. 1a, b. An electron bunch with 300 fC charge is generated by a radiofrequency photoelectron gun (GUN in Fig. 1a) and boosted to 8 MeV by a resonant accelerating cavity (LINAC). The beam is then focused by a solenoid magnet to a root-mean-square (RMS) spot size of $\sigma_{x,y} \approx 10$ μm, and propagated through the DLA. The laser is polarized along the electron axis z with field amplitude E_0, full-width-half maximum (FWHM) duration $\tau = 45$ fs, and wavelength $\lambda = 800$ nm. As shown in the expanded schematic of Fig. 1b, the nearly plane-wave field of the drive laser propagates through $D = 499$ μm of fused silica substrate and diffracts off of the grating layer with period $\lambda_g = 800$ nm into a set of evanescent longitudinal modes (shown by the inset color contour plot), one of which resonantly exchanges energy with the electrons inside the vacuum gap $g = 400$ nm. Resonant matching of the particle velocity to the phase velocity of the mode is accomplished by fine-tuning the laser's incidence angle as explained in the Methods section. Since $\sigma_{x,y} \gg g$, most of the electrons strike the fused silica substrate (with a median energy loss of 290 keV), while 1–2% are transmitted through the vacuum gap and propagate downstream. The energy spectra of the transmitted electrons is then measured with a magnetic spectrometer.

A representative spectrum, corresponding to an incident field $E_0 = 7$ GV m^{-1}, is shown in Fig. 1c. When the interaction is turned off by blocking the laser, the electron spectrum is narrow (black curve) and when the laser is present, the spectrum is broadened by the strong longitudinal fields excited inside the DLA (blue curve). The effect of the DLA can be isolated by deconvolving each "laser-on" shot with a representative "laser-off" shot, as shown in Fig. 1d, revealing a distinctive lineshape: the two peaks at ±18.5 keV correspond to electrons at the phases corresponding to peak acceleration and peak deceleration, while the peak at zero is caused by electrons, which did not overlap with the laser field. This symmetric arrangement is characteristic of an electron beam that is long compared to the optical period of the laser, since electrons then enter the DLA at all optical phases. Since the measurement of the peak location can be noisy, a maximal energy gain $\Delta E_{\max}$ is defined such that 75% of the charge is contained in the region $|\Delta E| \leq \Delta E_{\max}$.

Observation of nonlinear dephasing. We test the scaling of $\Delta E_{\max}$ vs E_0 by varying the laser field strength as shown in Fig. 1e. From $E_0 = 0$ to $E_0 \approx 6$ GV m^{-1} we observe that the maximum electron energy gain scales linearly with the incident field strength, while above 6 GV m^{-1} the energy gain saturates, and further increases in drive power reduce the energy gain.

To fully understand this behavior, we have to look closely at the relation between the maximum energy gain and the peak axial accelerating field in the structure. If the DLA exhibits a purely linear dielectric response, the average accelerating gradient (energy gain per unit of propagation distance) experienced by an optimally phased test particle of charge q injected at the peak of the laser field scales linearly with the incident electric field: $G_0 = \kappa q E_0$. The "structure factor" κ is a dimensionless constant determined by the geometry and dielectric constant of the structure. The energy gain of an arbitrary test particle also depends on the complex spatial envelope of the laser field $\mathcal{E}(\mathbf{r}, t)$, which we normalize to have a peak magnitude of 1 at the input to the structure. Assuming the laser pulse duration (rather than the structure length) limits the interaction, neglecting the small y dependence of fields in the vacuum gap, and assuming linear trajectories, the energy gain of a test particle injected at phase ϕ_0 and velocity vector $\boldsymbol{\beta}c$ is given by:

$$\Delta E = G_0 \cos(\phi_0) \left| \int_C \mathcal{E}(\mathbf{r}, t) \mathrm{d}s \right|, \quad (1)$$

where the integral is taken along the particle trajectory C parametrized by its path length s: $\mathbf{r} = \mathbf{r}_0 + (\boldsymbol{\beta}/\beta)s$, $t = s/\beta c$. We note that there is also an implicit dependence in Eq. (1) on the particle's initial position $\mathbf{r}_0$, which becomes relevant when the transverse extent of the electron beam is taken into account.

We can heuristically understand the saturation in Fig. 1e by considering that increasing the pulse energy introduces an additional phase term $e^{i\Delta\phi}$ in $\mathcal{E}$ because the laser must propagate through a distance $D = 499$ μm of fused silica wafer where it excites a third-order nonlinear polarization field. The primary effect of the nonlinear response is an intensity-dependent phase modulation $\Delta\phi \approx n_2 k I D$, where I is the field intensity, $k = \omega/c$ is

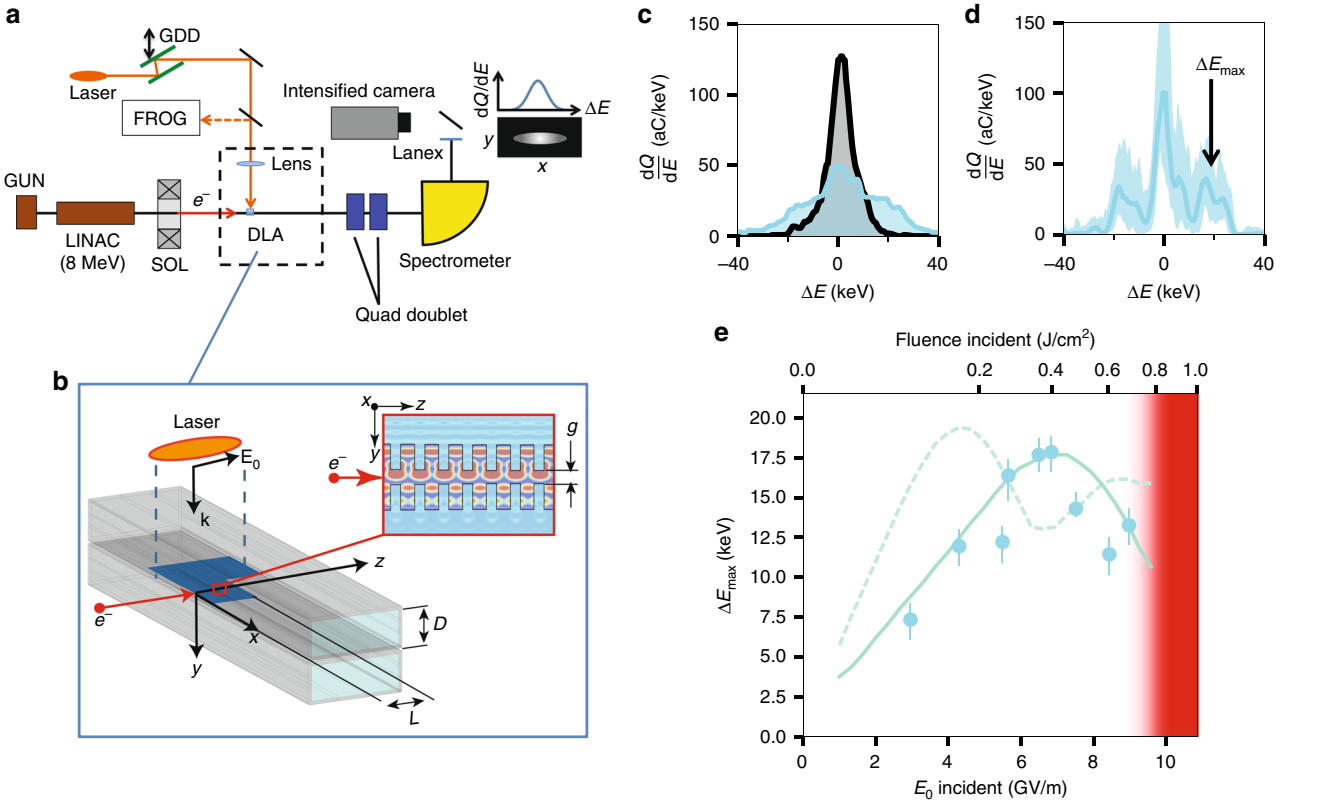

Fig. 1 Electron based measurement of the accelerating field in a DLA. **a** Experimental setup (not to scale). The electrons are pre-accelerated by a radio-frequency accelerator (GUN, LINAC) to 8 MeV energy, and focused into the DLA by a solenoid magnet (SOL). After the electrons interact with the DLA they are dispersed by a magnetic spectrometer and their energy spectra recorded. The incident laser group delay dispersion (GDD) is adjusted by an upstream grating compressor (green). **b** Schematic of the DLA showing the relationship between the drive laser, electron beam, and the grating teeth. **c** Electron energy distribution at the spectrometer screen for typical laser-on (blue) and laser-off (black) shots. Both spectra contain a total charge of nearly 3 fC. **d** Deconvolution of the two spectra in **c**. The shaded region bounds the variation caused by jitter as judged by de-convolving the on-shot in (**c**) with many independent off-shots. **e** Maximum energy gain as function of the drive laser energy (error bars indicate a 70% confidence interval accounting for jitter in both time-of-arrival and the laser-off distribution). Simulated energy gains (green) are shown for an on-axis particle (dashed) and averaged over many particles in a beam (solid). In all cases saturation is caused by dephasing while the accelerating field continues to increase linearly to 1.8 GV m^{-1} before nearing the damage threshold (red)

the laser wavenumber, and $n_2 = 2.48 \times 10^{-16}$ cm^2 W^{-1}[17] is the nonlinear refractive index, consistent with an independently measured z-scan[18] through the substrate. In a simplified picture, this self-phase modulation works to saturate the energy gain by forcing an otherwise synchronous electron to sample a changing phase. For $E_0 = 6$ GV m^{-1}, $\Delta\phi > \pi$, causing the sign of the field to flip and effectively halting the acceleration. Since the saturation can be explained by inclusion of a Kerr dephasing term in $\mathcal{E}$, the peak axial field in the structure is $\kappa E_0 = 1.8 \pm 0.3$ GV m^{-1} for the highest incident field ($E_0 = 9$ GV m^{-1}) in Fig. 1e. The value $\kappa = 0.2$ is obtained by fitting the data to simulation as explained in the next section. Due to the nonlinear saturation, the corresponding average gradient is $\bar{G} = \Delta E_{\max}/L_{\text{eff}} = 850$ MeV m^{-1} where L_{eff} is an effective interaction length (see Methods for discussion).

Simulations using measured input laser profiles. The effect of the nonlinear material response on the DLA energy gain is simulated in three steps (Fig. 2a): first, the incident amplitude and phase (up to a time-reversal ambiguity) are reconstructed from a frequency resolved optical gating (FROG) measurement upstream of the DLA; second, that reconstructed beam envelope is numerically propagated through 499 μm of silica by solving a generalized nonlinear Schrödinger equation (NLSE) (see Methods) using a split-step Fourier solver on an adaptive grid[19]; and finally the grating layer is simulated by the commercial finite-difference time domain (FDTD) code Lumerical[20], using the output of the NLSE as a source.

At low intensities the NLSE reduces to linear dispersion, but at high intensities it predicts significant nonlinear contributions, which can saturate the energy gain. The simulation includes self-focusing, self-steepening, Raman scattering[21] and multiphoton absorption[22]; but at moderate intensities the dominant feature is the intensity-dependent phase modulation (Kerr effect). This is illustrated in Fig. 2b, c, which show respectively the measured envelope of the laser used as input to the simulation and the corresponding output of the NLSE for $E_0 = 4.75$ GV m^{-1}. Self-focusing is evident in the increased amplitude (blue curve) of $\mathcal{E}(t)$ in Fig. 2b, while the effects of self-steepening and multiphoton absorption are not noticible. Free carrier generation is not included in the propagator, because a post-hoc calculation of the free carrier density[23,24] suggests that the induced phase change is negligible compared to the Kerr effect until very near the damage threshold.

Nonlinear effects are not significant in the thin layer around the grating, and moreover the FDTD results show that the grating layer preserves the complex amplitude and phase from the NLSE (up to a scale factor in amplitude and an offset in phase). This is shown in Fig. 2d by comparing the waveform input at the grating layer to the waveform evaluated in the center of the vacuum gap. The input and output pulses are nearly identical except for a

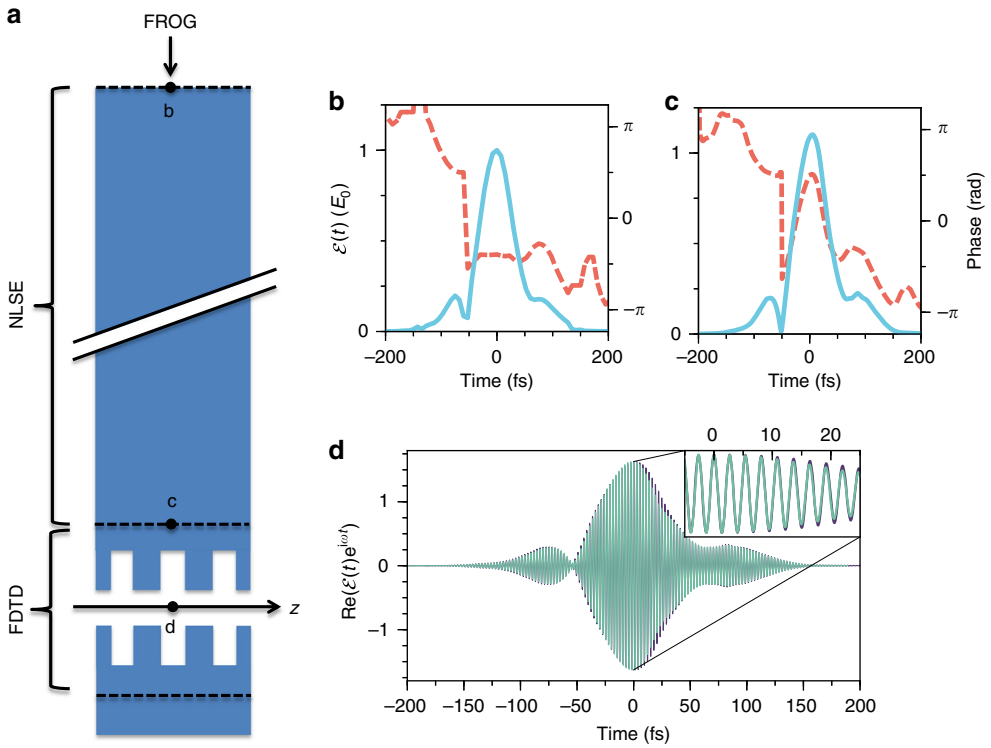

Fig. 2 Illustration of the simulation process. **a** Dashed lines delineate the three regions used in the simulation process (dots indicate the location where panels **b**–**d** were evaluated). **b** The simulations are initialized using a FROG measurement of the amplitude (solid) and phase (dashed) of the electric field before the DLA. The measurement shows a central peak of FWHM 45 fs with satellite lobes caused by residual third-order and higher dispersion terms. **c** The field envelope after propagation through the bulk layer of fused silica is then calculated by solving the NLSE for $E_0 = 4.75$ GV m^{-1}. **d** Finally, the area around the grating is simulated using an FDTD simulation initialized using the waveform from (**b**). Comparison of the input waveform (dark purple) with that in the vacuum gap (light green) demonstrates that the temporal structure is largely preserved. The input waveform has been scaled in amplitude and offset in phase to aid the comparison

small delayed reflection, which is a consequence of the fact that the bandwidth of the laser remains smaller than the bandwidth of the accelerator[25]. Thus it is a good approximation to bypass the computationally intensive simulation of the grating layer and directly use the pulse envelope at the entrance of the grating layer to track particles using Eq. (1), with the calculated κ ranging from 0.18 to 0.23 depending on the relative longitudinal alignment of the two grating layers.

Tracking an ensemble of particles through Eq. (1) with $\mathcal{E}$ determined by the NLSE yields a prediction we can compare to the measured energy gain. We simulate two cases, shown as green curves in Fig. 1e: the first uses a single electron and perfect alignment between the laser, electron, and DLA (dashed green line); while the second averages over a realistic electron beam distribution ($\sigma_x = 10$ μm) having a typical misalignment ($x_0 = 10$ μm, $\beta_y/\beta_z = 5$ mrad) within the experimental tolerances. In both cases $\Delta E_{\max}$ rises linearly before saturating, but because the drive laser is narrowly focused, some electrons in the realistic beam see a lower field and saturate at a higher incident E_0. Once most individual trajectories have reached saturation, $\Delta E_{\max}$ plateaus at a level determined primarily by κ and n_2, nearly independent of alignment (the difference in the maxima of the two curves in Fig. 1e is less than 10%), from which we measure $\kappa = 0.2 \pm 0.04$, which is within the range of κ values independently simulated from FDTD simulations, and is consistent with prior experiments using similar structures[3].

Compensation of nonlinear dephasing. The study of soliton solutions for nonlinear optics[21] suggests that negative group delay dispersion (GDD) can effectively compensate the observed dephasing by providing an opposite phase curvature to cancel the effects of nonlinear propagation, as illustrated in Fig. 3a. In soliton propagation, the Kerr phase is exactly balanced by material dispersion to create a stationary pulse. In fused silica (at $\lambda = 800$ nm) we cannot propagate a soliton, but we can "pre-compensate" the Kerr phase by applying anomalous dispersion with a grating compressor at the output of the chirped pulse amplification system upstream of the DLA (shown in green at the top of Fig. 1a). This is opposite of a common pulse shaping technique, in which a compressor is used after a nonlinear medium to shorten the pulse length.

Anomalous dispersion stretches the pulse length τ and introduces a quadratic temporal phase dependence (i.e., chirp), which can approximately cancel the Kerr phase modulation. The lengthening of the pulse lowers the incident field ($E_0 \propto \tau^{-1/2}$) but increases the interaction length ($L_{\text{eff}} \propto \tau$), yielding a net energy gain ($\Delta E \propto \tau^{1/2}$). If the Kerr effect isn't exactly compensated by the chirped laser pulse, the residual phase variation causes the particles to lose synchronicity, which we can illustrate by re-writing Eq. (1) in the Fourier domain:

$$\Delta E = G_0 \cos(\phi_0) \left| \int_C \mathcal{F}\left[\tilde{\mathcal{E}}(\mathbf{k}, \omega)\right] \mathrm{d}s \right|. \qquad (2)$$

Here $\tilde{\mathcal{E}}(\mathbf{k}, \omega)$ is the Fourier transform of the field (along the electron trajectory C), and $\mathcal{F}$ is the Fourier transform operator. By exchanging the order of integration we find a Dirac delta function enforcing the plane-wave phase matching condition:

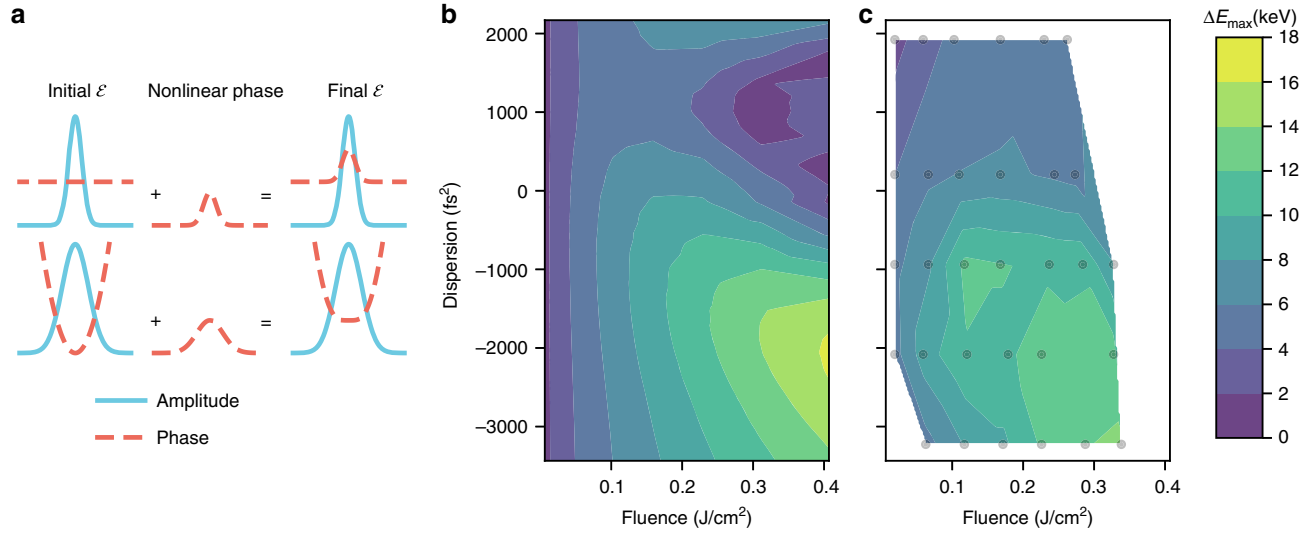

Fig. 3 Compensation of nonlinear dephasing by tuning the laser phase. **a** Cartoon showing how additional dispersion (bottom row) can flatten the phase and thus increase the energy gain. **b** Theoretical energy gain as a function of fluence and dispersion (as determined at the entrance to the fused silica wafer). **c** Measured energy gain (sampled at the location of the dots) at the same conditions as in (**b**)

$\delta(\omega_0 - \omega)$, where $\omega_0 \equiv k_g \beta c$. We thus arrive at a simple expression for the energy gain in terms of the laser spectrum:

$$\Delta E \propto G_0 \cos(\phi_0) \left| \tilde{\mathcal{E}}(\omega = \omega_0) \right| \quad (3)$$

which shows that the energy gain is proportional to the phase-matched (ω_0) frequency component of the laser electric field. Note that we have ignored the angular distribution of the drive laser wavenumbers **k**, inclusion of which would result in blurring the Dirac delta function over a bandwidth ≈1 nm. From this formulation, it follows that dispersion (which does not alter the bandwidth of the laser) will not change the energy gain of the DLA by itself. Self-phase modulation, however, changes the bandwidth of the pulse by applying a nonlinear phase in the time domain so that the initial dispersion becomes a sensitive parameter for a high intensity drive laser.

Such behavior fully supported by the pulse propagation and particle tracking calculations show in Fig. 3b, and is well reproduced in experimental measurements (see Fig. 3c). At low fluences, decreasing the dispersion has no effect; while for high fluences, decreasing the dispersion results in a rapid increase in energy gain. The dispersion is adjusted by changing the spacing between compressor gratings (marked "GDD" in Fig. 1a), and the "zero-dispersion" point is established by maximizing second harmonic generation from a thin BBO crystal located in the same plane as the DLA. The data here are recorded using a DLA with a $g = 800$ nm vacuum gap (having smaller κ and larger transmission than the 400 nm gap of Fig. 1b) in order to increase the signal-to-noise ratio of the energy spectra. As in Fig. 1e, the differences between the simulation and measured data can be attributed to uncertainty in the electron beam parameters and alignment of the laser. Nonetheless, the agreement over the wide available range of parameters in the fluence/dispersion scan demonstrates the importance of phase and amplitude control of the incident laser field for accelerator optimization.

Discussion

We have used 45 fs laser pulses to drive a fused silica dual-grating DLA up to incident fields of 9 GV m^{-1}, which is shown to excite a 1.8 GV m^{-1} accelerating mode. At these high field intensities, we have observed for the first time the breaking of phase synchronicity of the laser field with the electrons due to the the direct influence of nonlinear optical properties of the dielectric structure, which lowers the effective accelerating gradient to 850 MeV m^{-1}. Through comparison with detailed numerical simulation of the experiment, the dominant nonlinear effect is found to be a temporally varying Kerr phase shift, which produces a fully reversible saturation of the observed energy gain. This effect is shown to be mitigated by chirping the laser pulse prior to the structure, and thereby inducing a compensating phase profile that counteracts the nonlinear phase shift. We have thereby demonstrated the effectiveness of phase and amplitude control of the incident laser field as a method of keeping the electrons synchronous with the accelerating wave over many periods.

Our work highlights the characteristic sensitivity of the DLA to pulse shaping of the drive laser. While other laser accelerators, such as laser plasma wakefield accelerators, are mostly sensitive to the pulse envelope, the beam dynamics in DLAs are directly dependent on both the intensity and phase of the drive laser pulse. This offers an extra degree of freedom for controlling the beam dynamics over significant lengths. For example, more complex manipulation of the laser pulse could be used to create alternate gradient focusing[26–28], or as a means of changing the resonant velocity. Our results also indicate that mitigation of nonlinear optical effects, for example by using thinner substrates or pre-compensating with anomalous dispersion, should be taken into account in proposed multi-stage on-chip systems, where the propagation distances and field intensities in optical delivery waveguides will be of similar magnitude to those in the present experiment[29].

Methods

Dual-grating structure. The accelerating structure consists of two gratings made by etching teeth 700 nm tall by 325 nm wide with 800 nm periodicity into 500 μm thick (y direction) fused silica wafers. The wafers are then bonded together to leave either a 400 or 800 nm vacuum channel[30,31]. The gratings were made 0.5 or 1 mm long in z (the periodic direction) and 0.5 mm wide in x (parallel to the teeth), as shown in the inset of Fig. 1b.

The DLA diffracts the incident electric field E_0 into a set of Bloch harmonics[32] (indexed by integer n) propagating inside the vacuum channel with wavenumbers $k_n = k_0 + nk_g$, where $k_0 = (\omega/c)\sqrt{\epsilon}\sin\theta$ is the projection of the incident laser wavenumber onto the z axis, $k_g = 2\pi/\lambda_g$, ω is the natural frequency of the laser, ϵ is the dielectric constant, and θ is the laser incidence angle measured from normal. A given mode can resonantly interact with electrons of velocity βc if the phase

matching condition $k_n - \omega/\beta c = 0$ is satisfied. The structures used in this experiment are designed for operation in the fundamental mode ($n = 1$) with $\beta = 1$ electrons. For 8 MeV electrons of $\beta \approx 0.998$, we align the back-reflection of the laser off of the grating surface and set $\theta = 1.2$ mrad to tune the phase-matching condition so that Eq. (3) will pick out the central frequency component.

Drive laser. The drive laser is a commercial Ti:sapphire system producing a few mJ pulses with ≈25 nm bandwidth and a FWHM pulse duration of 45 fs. A portion of the laser is split off and frequency tripled to drive the electron gun photocathode, while the remainder is propagated downstream to the DLA. The transverse beam profile at the DLA ($1/e^2$ dimensions $w_x = 45$ μm and $w_z = 500$ μm) is measured using a charge-coupled device, and the temporal profiles are measured upstream of the DLA using a FROG, as shown in Fig. 1a, with example trace shown in Fig. 2a. The incident field E_0 is calculated from the pulse energy measured after the DLA, assuming there is negligible longitudinal-to-transverse coupling.

GDD of the drive laser is controlled by adjusting a grating compressor located at the end of a commercial chirped pulse amplification module (labeled "GDD" in Fig. 1a). The change in dispersion as a function of the grating spacing can be calculated[33] and compares well with FROG measurements. To determine the dispersion in absolute units it is necessary to account for the difference between the FROG and the DLA optical paths. This is done in the experiment by comparing the dispersion required to minimize pulse duration at both locations. For this, the DLA is temporarily replaced with a barium borate (BBO) crystal and the second harmonic generation signal is maximized, with minimal pulse length corresponding to maximal intensity.

Electron-laser alignment. The electron bunch is spatially overlapped with the laser on a phosphor screen angled at 45° (relative to z and y). The laser $1/e^2$ spot size ($w_x = 45$ μm) is similar in magnitude to the electron beam RMS size ($\sigma_x = 10$ μm) and pointing jitter (also 10 μm). Consequently, in the simulation of Fig. 1e (solid line) the relative overlap of the two beams must be taken into account. Time-of-arrival is synchronized by using the laser to ablate a copper grid, creating an electron gas at its surface with a rapid formation time (<1 ps) and a slow dissipation time (~15 ps), which interacts strongly with the electron beam[34]. The interaction is easily detected when it distorts a point-projection image of the grid (formed by focusing the electron beam before the grid). After co-aligning the beams in space and time the DLA is inserted and adjusted (by in-vacuum motors) to maximize electron beam transmission, first through 100 and 50 μm alignment channels and then through the vacuum gap of the accelerator.

Spectral measurement. Electron spectra are recorded by measuring the beam profile around the bend of a round-pole magnetic spectrometer. The magnetic dispersion (11 cm) is small enough that we cannot resolve the intrinsic energy spread of the bunch (<1 keV), and instead see a beam that appears 3 keV wide (black histogram in Fig. 1a). The extra width comes from the point-spread function of our camera and fluorescent screen, and thus is largely free of beam jitter, making the "laser-off" spectra consistent from shot-to-shot. This makes it easy to subtract their contribution to the "laser-on" spectra by deconvolution. Direct deconvolution (in the Fourier domain) is very sensitive to noise in the tails of distributions (due to division by zero), so we use an iterative Richardson-Lucy type algorithm. Applying our algorithm to any two "off-shots" yields spectral widths of <3 keV, which can be taken as a bound on minimum effect that can be reliably measured.

Average gradient. An average gradient for an accelerator is typically defined as the energy gain divided by the length of the accelerating structure. Since the interaction in our structure is limited by the laser pulse width τ, the effective length of the interaction must be calculated from the laser profile as in Eq. (1):

$$L_{\mathrm{eff}} \equiv \left| \int_C \mathcal{E}(\mathbf{r}, t) \mathrm{d}z \right| \tag{4}$$

where the trajectory C is taken along the z axis. Using $\mathcal{E}$ from the FROG we get $L_{\mathrm{eff}} = 21.5$ μm. For the maximum observed energy gain of $\Delta E_{\max} = 18$ keV the average gradient is $\bar{G} = \Delta E_{\max}/L_{\mathrm{eff}} = 850$ MV m^{-1}. If there were no nonlinear distortion of the pulse, we see from Eqs. (1) and (4) that the average gradient defined in this way would then equal the linear field gradient $G_0 = \kappa q E_0$ (with values as high as 1.8 GeV m^{-1}).

Nonlinear propagation. To model nonlinear propagation in bulk fused silica we solve a generalized nonlinear Schrödinger equation (NLSE) using a split-step Fourier algorithm[21,22]. A pulse propagating in the $\hat{y}$ direction is represented as $A(\mathbf{r}, t)\mathrm{e}^{\mathrm{i}(k_0 y - \omega_0 t)}$, where the complex envelope A can take on complex values, but is assumed to vary slowly relative to the optical fields. In a nonlinear medium this envelope evolves according to:

$$\frac{\partial A}{\partial y} = \left[\hat{D}_f + \hat{D}_s + \hat{N}\right] A \tag{5}$$

Table 1 Table of model inputs

Parameter	Value	Notes
Material	SiO_2	
n_0	1.45	
n_2	2.45×10^{16} cm^2/W	17
$k^{(2)}$	36.163 fs^2/mm	
κ	10×10^{-6} 1/cm	
β_6	5×10^{-83} m^9/W^6	22
T_R	3 fs	21
λ	800 nm	
w_x	45 μm	Gaussian
w_z	500 μm	Gaussian
τ	45 fs	FROG trace
Pulse energy	2–200 μJ	

where $\hat{D}_f, \hat{D}_s, \hat{N}$ are the diffraction, dispersion, and nonlinear operators, respectively:

$$\hat{D}_f = \frac{i\lambda}{4\pi n_0}\left(1 - \frac{i\lambda}{2\pi c}\partial_t\right)\left(\partial_x^2 + \partial_z^2\right) \tag{6}$$

$$\hat{D}_s = -\frac{i}{2}k^{(2)}\partial_t^2 - \frac{1}{2}\xi \tag{7}$$

$$\hat{N} = \frac{i2\pi n_2}{\lambda}|A^2| - \frac{1}{A}\left(\frac{n_2}{c}\right)\partial_t\left(A|A^2|\right) - \frac{i2\pi n_2}{\lambda}T_R\partial_t|A^2| - \frac{\beta_6}{2}|A^{10}| \tag{8}$$

Note that the equations are written in the moving frame, $t = t_0 - y/v_g$, and include dispersion $k^{(2)}$, absorption ξ, six-photon absorption β_6, and third-order polarization n_2, with a linearized Raman response T_R.

Given an initial field profile $A(\mathbf{r} = 0, t = 0)$, the field after 499 μm of glass is calculated via a finite difference approach to Eq. (5). The propagation is implemented using the "Generalised Adaptive Fast-Fourier Evolver" (GAFFE)[19], which uses a split-step Fourier solver and an adaptive grid in order to rapidly compute the right hand side of Eq. (5) without aliasing.

The model inputs for these simulations are cataloged in Table 1. Note that the 6-photon cross section may be calculated from the Keldysh formula in the low intensity limit or fit to give an effective value at intermediate intensities[22,23].

For the relevant initial conditions we find that Kerr self-phase-modulation is the primary nonlinear phenomenon, followed by self-focusing and then six-photon absorption and self-steepening. Figure 2b shows the propagation of the envelope in Fig. 2a through 499 μm of fused silica for a peak field of 4.75 GV m^{-1}. Self-phase modulation is evident in that the phase (dotted) follows the intensity (the square of the illustrated electric field). Self-focusing is also evident in that the peak of the envelope in Fig. 2b exceeds that of Fig. 2a. Self-steepening is barely visible, but begins to present itself more prominently as E_0 increases. Similarly, the 6-photon absorption begins to erode energy from the peak which alters the onset of filamentation in the pulse.

The generation of free carriers[23] is neglected in Eq. (5), because post-hoc estimates suggest that the change in index of refraction n due to free carriers is a small fraction of the contribution due to self-phase modulation. At $E_0 = 5$ GV m^{-1}, where self-phase modulation saturates the DLA interaction, multi-photon absorption is still the dominant mechanism (the Keldysh parameter is $\gamma \approx 3$) and the maximum electron density is estimated to be less than 1×10^{15} cm^{-3}, which would cause a change in n of 0.025%. For $E_0 > 10$ GeV m^{-1} the free-carrier population begins to become significant (but now increasing as ~I^4), which likely contributes to the observed damage threshold around that intensity.

Data availability. The datasets generated during and analyzed during the current study are available from the corresponding author on reasonable request.

Received: 4 December 2017 Accepted: 16 July 2018
Published online: 17 August 2018

References

1. England, R. J. et al. Dielectric laser accelerators. *Rev. Mod. Phys.* **86**, 1337–1389 (2014).
2. Mourou, G., Brocklesby, B., Tajima, T. & Limpert, J. The future is fibre accelerators. *Nat. Photon.* **7**, 258–261 (2013).

3. Wootton, K. P., McNeur, J. & Leedle, K. J. Dielectric laser accelerators: designs, experiments, and applications. *Rev. Accel. Sci. Technol.* **9**, 105–126 (2016).
4. Rosenzweig, J. B. et al. The GALAXIE all-optical FEL project. *AIP Conf. Proc.* **1507**, 493–498 (2012).
5. Bar-Lev, D. & Scheuer, J. Plasmonic metasurface for efficient ultrashort pulse laser-driven particle acceleration. *Phys. Rev. ST Accel. Beams* **17**, 121302 (2014).
6. Simakov, E. I., Andrews, H. L., Herman, M. J., Hubbard, K. M. & Weis, E. Diamond field emitter array cathodes and possibilities of employing additive manufacturing for dielectric laser accelerating structures. *AIP Conf. Proc.* **1812**, 060010 (2017).
7. Peralta, E. A. et al. Design, fabrication, and testing of a fused-silica dual-layer grating structure for direct laser acceleration of electrons. *AIP Conf. Proc.* **1507**, 169 (2012).
8. Ceballos, A *et al.* Fabrication and demonstration of a silicon buried grating accelerator *Proceedings of the 6th International Particle Accelerator Conference*. WEPJE021 (JACoW, Geneva, Switzerland, 2015).
9. Peralta, E. A. et al. Demonstration of electron acceleration in a laser-driven dielectric microstructure. *Nature* **503**, 91–94 (2013).
10. Breuer, J. & Hommelhoff, P. Laser-based acceleration of nonrelativistic electrons at a dielectric structure. *Phys. Rev. Lett.* **111**, 134803 (2013).
11. McNeur, J. et al. A miniaturized electron source based on dielectric laser accelerator operation at higher spatial harmonics and a nanotip photoemitter. *J. Phys. B: At. Mol. Opt. Phys.* **49**, 034006 (2016).
12. Leedle, K. J. et al. Dielectric laser acceleration of sub-100 keV electrons with silicon dual-pillar grating structures. *Opt. Lett.* **40**, 4344–4347 (2015).
13. Leedle, K. J., Pease, R. F., Byer, R. L. & Harris, J. S. Laser acceleration and deflection of 963 keV electrons with a silicon dielectric structure. *Optica* **2**, 158–161 (2015).
14. Wootton, K. P. et al. Demonstration of acceleration of relativistic electrons at a dielectric microstructure using femtosecond laser pulses. *Opt. Lett.* **41**, 2696–2699 (2016).
15. Maxson, J. et al. Direct measurement of sub-10 fs relativistic electron beams with ultralow emittance. *Phys. Rev. Lett.* **118**, 154802 (2017).
16. Koyama, K., Otsuki, S., Uesaka, M., Yoshida, M. & Aimidula, A. Parameter study of a laser-driven dielectric accelerator for radiobiology research. *J. Phys. B: At. Mol. Opt. Phys.* **47**, 234005 (2014).
17. Milam, D. Review and assessment of measured values of the nonlinear refractive-index coefficient of fused silica. *Appl. Opt.* **37**, 546–550 (1998).
18. Sheik-Bahae, M., Said, A. A., Wei, T. H., Hagan, D. J. & Stryland, E. W. V. Sensitive measurement of optical nonlinearities using a single beam. *IEEE J. Quantum Electron.* **26**, 760–769 (1990).
19. Grace, E. GAFFE A toolbox for solving evolutionary nonlinear PDEs (2009). URL https://www.mathworks.com/matlabcentral/fileexchange/24016-gaffe-a-toolbox-for-solving-evolutionary-nonlinear-pdes.
20. FDTD solutions | Lumerical's nanophotonic FDTD simulation software. URL http://www.lumerical.com/tcad-products/fdtd/.
21. Agrawal, G. in *Nonlinear Fiber Optics*. 5th edn, Ch. 2 (Academic Press, Boston, 2013)..
22. del Hoyo, J. et al. Rapid assessment of nonlinear optical propagation effects in dielectrics. *Sci. Rep.* **5**, 7650 (2015).
23. Sudrie, L. et al. Femtosecond laser-induced damage and filamentary propagation in fused silica. *Phys. Rev. Lett.* **89**, 186601 (2002).
24. Schiffrin, A. et al. Optical-field-induced current in dielectrics. *Nature* **493**, 70–74 (2012).
25. Soong, K. et al. Electron beam position monitor for a dielectric microaccelerator. *Opt. Lett.* **39**, 4747–4750 (2014).
26. Rosenzweig, J. & Serafini, L. Transverse particle motion in radio-frequency linear accelerators. *Phys. Rev. E* **49**, 1599–1602 (1994).
27. Naranjo, B., Valloni, A., Putterman, S. & Rosenzweig, J. B. Stable charged-particle acceleration and focusing in a laser accelerator using spatial harmonics. *Phys. Rev. Lett.* **109**, 164803 (2012).
28. Niedermayer, U., Egenolf, T. & Boine-Frankenheim, O. Beam dynamics analysis of dielectric laser acceleration using a fast 6d tracking scheme. *Phys. Rev. Accel. Beams* **20**, 111302 (2017).
29. Hughes, T. W. et al. On-chip laser power delivery system for dielectric laser accelerators. *Phys. Rev. Appl.* **9**, 054017 (2018).
30. Peralta, E. A. *Accelerator on a Chip Design, Fabrication, and Demonstration of Grating-Based Dielectric Microstructures for Laser-Driven Acceleration of Electrons*. Ph.D. thesis. Stanford University (2015).
31. Plettner, T., Lu, P. P. & Byer, R. L. Proposed few-optical cycle laser-driven particle accelerator structure. *Phys. Rev. ST Accel. Beams* **9**, 111301 (2006).
32. Joannopoulos, J., Johnson, S. G., Winn, J. N. & Meade, R. D. *Photonic Crystals*, 2nd edn (Princeton University Press, New Jersey, 2008).
33. Treacy, E. Optical pulse compression with diffraction gratings. *IEEE Quantum Opt.* **5**, 454–458 (1969).
34. Scoby, C. M., Li, R. K. & Musumeci, P. Effect of an ultrafast laser induced plasma on a relativistic electron beam to determine temporal overlap in pump–probe experiments. *Ultramicroscopy* **127**, 14–18 (2013).

Acknowledgements

We thank Robert L. Byer, James Harris, and Huiyang Deng for helpful discussions. This work was supported in part by the Gordon and Betty Moore Foundation under grant GBMF4744 (Accelerator on a Chip) and by the U.S. Department of Energy, Office of Science, under contract numbers DE-AC02-76SF00515 and DE-SC0009914. This material is based upon work supported in part by the National Science Foundation under grants PHY-1734215 and PHY-1535711.

Author contributions

P.M. and R.J.E. proposed and supervised the acceleration experiment. D.C., S.C., J.M., P.M., X.S., E.T., R.J.E., A.H., I.V.M., K.P.W. and Z.W. performed the acceleration experiment. E.A.P. fabricated dielectric accelerator structures. K.P.W. measured phase distortion with FROG. D.C. analyzed data from the acceleration experiment. R.J.E. simulated the DLA in Lumerical. D.C. simulated nonlinear pulse propagation in GAFFE. The manuscript was prepared with input and comments from all authors.

Additional information

Competing interests: The authors declare no competing interests.